Land–Atmosphere Interactions during GRAINEX: Planetary Boundary Layer Evolution in the Presence of Irrigation

E. D. RAPPIN,[a] R. MAHMOOD,[b] U. S. NAIR,[c] AND R. A. PIELKE SR.[d,e]

[a] *Kentucky Climate Center, Western Kentucky University, Bowling Green, Kentucky*
[b] *High Plains Regional Climate Center, School of Natural Resources, University of Nebraska–Lincoln, Lincoln, Nebraska*
[c] *Department of Atmospheric Science, University of Alabama in Huntsville, Huntsville, Alabama*
[d] *Department of Atmospheric and Oceanic Sciences, University of Colorado Boulder, Boulder, Colorado*
[e] *Cooperative Institute for Research in Environmental Sciences, University of Colorado Boulder, Boulder, Colorado*

(Manuscript received 15 August 2021, in final form 20 April 2022)

ABSTRACT: This paper analyzed observations from the Great Plains Irrigation Experiment (GRAINEX) to better understand land–atmosphere (L–A) interactions and PBL evolution. This study is focused on a day when the largest forcing on the boundary layer originated from the land surface/land use. To examine these impacts, we also applied the Weather Research and Forecasting (WRF) Model. Results from the observations show that compared to nonirrigated areas, air temperature, wind speed, and PBL height (PBLH) were lower while dewpoint temperature and latent heat flux were higher over irrigated areas. Findings suggest that entrainment layer drying and differences in energy partitioning over irrigated and nonirrigated areas played an important role in PBL evolution. In the final hours of the day, the PBL collapsed faster over nonirrigated areas compared to irrigated. The WRF Model simulations agree with these observations. They also show that the extent of irrigation [expressed as irrigation fraction (IF)] in an area impacts L–A response. Under ~60% IF, the latent heat flux and mixing ratio reach their highest value while temperature and PBLH are at their lowest, and sensible heat flux is near its lowest value. Results are reversed for ~2% IF. It is concluded that irrigation notably impacts L–A interactions and PBL evolution.

KEYWORDS: Anthropogenic effects/forcing; Atmosphere-land interaction; Climate sensitivity; Soil moisture

1. Introduction

Globally, agriculture-related conversion of natural lands to croplands has increased rapidly and is particularly noticeable in the second half of the twentieth century (cf. Pielke et al. 2011). The Corn Belt of the central United States has observed a 400% increase in harvested corn in the 60 years from 1950 to 2010 (National Agricultural Statistics Service 2017). Due to increased demand for food, irrigation has become more widespread in the central United States as well. In Nebraska, acreage and production of irrigated soybean and corn cropland has increased roughly from 10% in 1950 to 60% in 2010 (National Agricultural Statistics Service 2017). As a result of land cover change and increased irrigation, the central United States has reported a 35% increase in precipitation and up to a 1°C decrease in temperature from 1910–49 to 1970–2009 (Alter et al. 2018), one of the largest such changes in the northern midlatitudes.

It is well known that land use and land cover (LULC) plays an important role in land–atmosphere (L–A) interactions and hence impacts weather and climate (Adegoke et al. 2007; Betts et al. 2007; Carleton et al. 2001; Mahmood et al. 2014; Gerken et al. 2019; LeMone et al. 2007; Pielke et al. 2007; Rabin et al. 1990; Segal et al. 1989; Zeng et al. 2016). These studies show LULC notably influences temperatures, moisture distribution, cloud development, and convective activities. Modifications of LULC [known as LULC change (LULCC)] further impacts these L–A interactions (Brovkin et al. 2013; Loveland and Mahmood 2014; Mahmood et al. 2010; Melillo et al. 2014; Meehl et al. 2014; Pielke et al. 2011, 2016; Pitman et al. 2009). Note that LULCC can result in deforestation leading to agricultural cropland and urbanization, conversion of natural grassland to cropland and urbanization, and establishment of man-made reservoirs.

LULCC and the expansion of agriculture around the world also modified weather and climate (e.g., Campra et al. 2008; Costa et al. 2007; He et al. 2020; Nikiel and Eltahir 2019; Puma and Cook 2010; Segal et al. 1989; Thiery et al. 2020). In many major agricultural regions of the world, irrigation was introduced to further increase food production. The addition of water in these regions has added another "layer" of complexity and magnified some of the atmospheric impacts of LULCC. Typical impacts of irrigation include, cooling of daily temperature (Yang et al. 2017; Chen and Dirmeyer 2020; Mahmood et al. 2006; Lawston et al. 2020), lowering of extreme maximum temperatures (Mahmood et al. 2004), increases in atmospheric moisture content (Mahmood et al. 2008; Xu et al. 2019), changes in precipitation amount and location (Barnston and Schickedanz 1984; DeAngelis et al. 2010; Devanand et al. 2019; Sen Roy et al. 2011; Wei et al. 2013; Yang et al. 2019), increased evapotranspiration (Chen and Dirmeyer 2020), enhanced latent heat flux (Q_e), and lowering of the sensible heat flux (Q_h) (Valmassoi et al. 2020). The North American Great Plains (GP) is an excellent example where widespread irrigation

Supplemental information related to this paper is available at the Journals Online website: https://doi.org/10.1175/JHM-D-21-0160.s1.

Corresponding author: Rezaul Mahmood, rmahmood2@unl.edu

DOI: 10.1175/JHM-D-21-0160.1

has been adopted for agriculture. The irrigation in this region is largely dependent on the Ogallala Aquifer, which is also known as the High Plains Aquifer. Atmospheric impacts of irrigation in this region can be found, for example, in the research by Mahmood and Hubbard (2002), Adegoke et al. (2003), DeAngelis et al. (2010), Lawston et al. (2015), and Szilagyi and Franz (2020).

In summary, irrigation modifies the soil moisture of the land surface which in turn impacts the surface energy and water budgets through changes to the albedo and Bowen ratio (the ratio of Q_h to Q_e) or evaporative fraction (ratio of Q_e to the net surface flux). The wetter the soil, the greater the incoming radiational energy is partitioned into evapotranspiration, leading to relatively smaller values of Q_h and a larger evaporative fraction. Depending on the specific humidity, evapotranspiration from moist soil can be static or change in magnitude over multiple time scales. In turn, the evaporative fraction exerts strong control on PBL growth and decay as the magnitude of the sensible heating controls its diurnal evolution. The strength and depth of PBL growth impacts entrainment from the free atmosphere which can subsequently influence the near-surface atmospheric properties through turbulent mixing. The above process chain succinctly describes L–A interactions (Van Heerwaarden et al. 2009; Santanello et al. 2009, 2011).

However, there is still a lack of observation-based research on irrigation impacts on near-surface meteorology and planetary boundary layer (PBL) development. To address this need we have conducted a field campaign known as the Great Plains Irrigation Experiment (GRAINEX) during the growing season of 2018. The GRAINEX field campaign is the first of its kind and focused on collecting atmospheric data from adjacent irrigated (IRR) and nonirrigated (NOIRR) areas in eastern Nebraska (Figs. 1a,b) (Rappin et al. 2021). The data show the most extensive irrigation lies just west of the Big Blue River (Figs. 1a,b) (Ozdogan and Gutman 2008; Salmon et al. 2015). Overall, southeastern Nebraska is one of the most extensively irrigated regions of the world (Johnson et al. 2011).

Previously, Rappin et al. (2021) provided detailed discussions on the GRAINEX field campaign, which include description of instrumentation, data collection efforts, summary of near-surface meteorology in the context of irrigated and nonirrigated land use, analysis of the PBL evolution using mixing diagram and vertical profiler data, and overall summary assessment of L–A interactions during the entire study period. The objectives of this study are to investigate L–A interactions and diurnal evolution of the PBL over IRR and NOIRR during the GRAINEX campaign. Specifically, this research determined the interactive role of moisture, heat flux, and entrainment layer on the diurnal evolution of the PBL over IRR and NOIRR. This study also quantified the extent of irrigation and its relationship with PBL development. To fulfill the objectives of this research, observational data from GRAINEX are analyzed and a series of model simulations are conducted. For numerical simulations, the Weather Research and Forecasting (WRF) Model is used. Thus, compared to Rappin et al. (2021), this study focuses solely on diurnal evolution of the PBL over irrigated and nonirrigated land use. In addition, this paper uses the WRF Model to assess L–A interactions and PBL evolution in the context of extent of irrigation. The observational dataset, specific study period, and model configuration are described in section 2. In section 3, PBL evolution is discussed. Section 4 examines the model results and concluding remarks are provided in section 5. Additionally, there is a 6-h lag in local standard time (LST) compared to UTC (LST = UTC − 6 h).

2. Data and numerical simulations

a. Observations

The field phase of GRAINEX took place in southeastern Nebraska (NE) over a ~100 × 100 km^2 area comprised of adjacent IRR and NOIRR croplands from the end of May until the beginning of August 2018 (Figs. 1a,b). Nebraska was chosen as it is one of the most highly irrigated regions of the world, and the most irrigated state in the United States. Two intensive observation periods (IOPs) were selected, and data collection was completed with extensive observational arrays. These IOPs are 1) 30 May 2018–13 June 2018 (IOP1) and 2) 16–30 July 2018 (IOP2). IOP1 represents a period when irrigation commonly begins while IOP2 represents a period in the growing season when crop-water demand is high and as a result, irrigation application is at a maximum. This period also represents enhanced L–A interactions. Extensive discussions of instrumentation are presented in Rappin et al. (2021). Here we discuss instrumentation that are only relevant to this study.

Observational platforms include 12 Integrated Surface Flux Systems (ISFS) and two Integrated Sounding Systems (ISS), and radiosondes from these two ISS sites. Details of the observations can be found at https://www.eol.ucar.edu/field_projects/grainex. ISFS stations collected heat flux data and standard above-surface mass, momentum, moisture, and radiation quantities from 12 locations where 6 represent IRR and 6 represent NOIRR land uses (Fig. 1a).

Each site recorded soil moisture, soil temperature, soil heat capacity, and soil heat flux data. All ISFS sites operated continuously from about mid-May through mid-August. Two ISS sites were instrumented to profile the atmosphere through in situ measurements and ground based remote sensing for investigating the response of PBL to irrigation (Figs. 1a,b). One of these sites was located in York, NE, a predominantly IRR region while a second site was located in Rogers Memorial Farm, east of Lincoln, NE (Figs. 1a,b), representing the NOIRR region of eastern NE. The ISS stations are equipped with wind and thermodynamic (RASS) profilers, ceilometer, and standard surface meteorological observations platforms. Additionally, both sites simultaneously launched radiosondes every two hours from sunrise (~0500 LST) to sunset (~1900 LST) resulting in 8 launches per site per day. The data were collected for both IOP1 and IOP2. In short, a comprehensive set of data were collected to understand properties and evolution of the boundary layer during the IOPs over IRR and NOIRR regions of the study domain.

b. Case days: Overall conditions during IOP1 and IOP2 and the basis for selection of specific days

The observed seasonal difference between key land surface and near-surface meteorological observations, averaged over

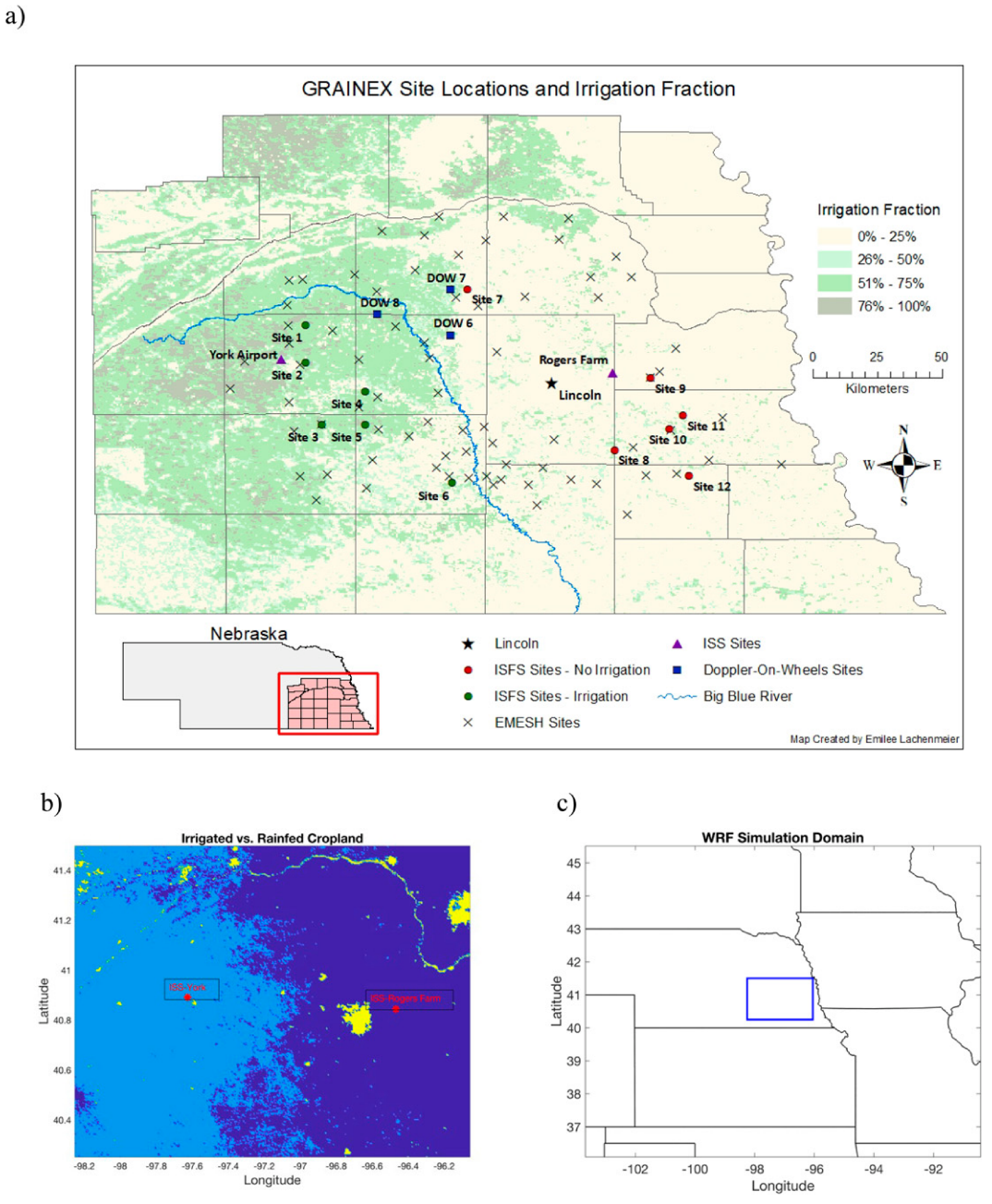

FIG. 1. (a) GRAINEX study area and observation platforms in southeastern Nebraska where the Big Blue River separates the irrigated and nonirrigated regions. (b) Cropland/land use where irrigated (light blue), rainfed (dark blue), and urban or river/lake (yellow); ISS sites denoted by * for spatial reference. (c) The modeling domains. (Modified from Rappin et al. 2021.)

IRR and NOIRR are displayed in Figs. 2a–c for 31 May 2018 through 30 July 2018. The differences in IRR and NOIRR 2-m temperature (Fig. 2a) shows a persistent higher temperature over NOIRR cropland that increases in magnitude as the growing season progresses. A statistically significant polynomial fit of the 2-m temperature yields the greatest rate in decline of the 2-m temperature difference (not shown). It occurred at the same time as the 2-m mixing ratio difference turns positive, around 1 July (Fig. 2b). The 2-m mixing ratio figure is indicative of a climatological specific-humidity pattern through June with a growing irrigation impact in July. The soil moisture difference time series (Fig. 2c; Fig. 1 in the online supplemental material) shows a strong irrigation signal in July, as seen in the high-frequency oscillations

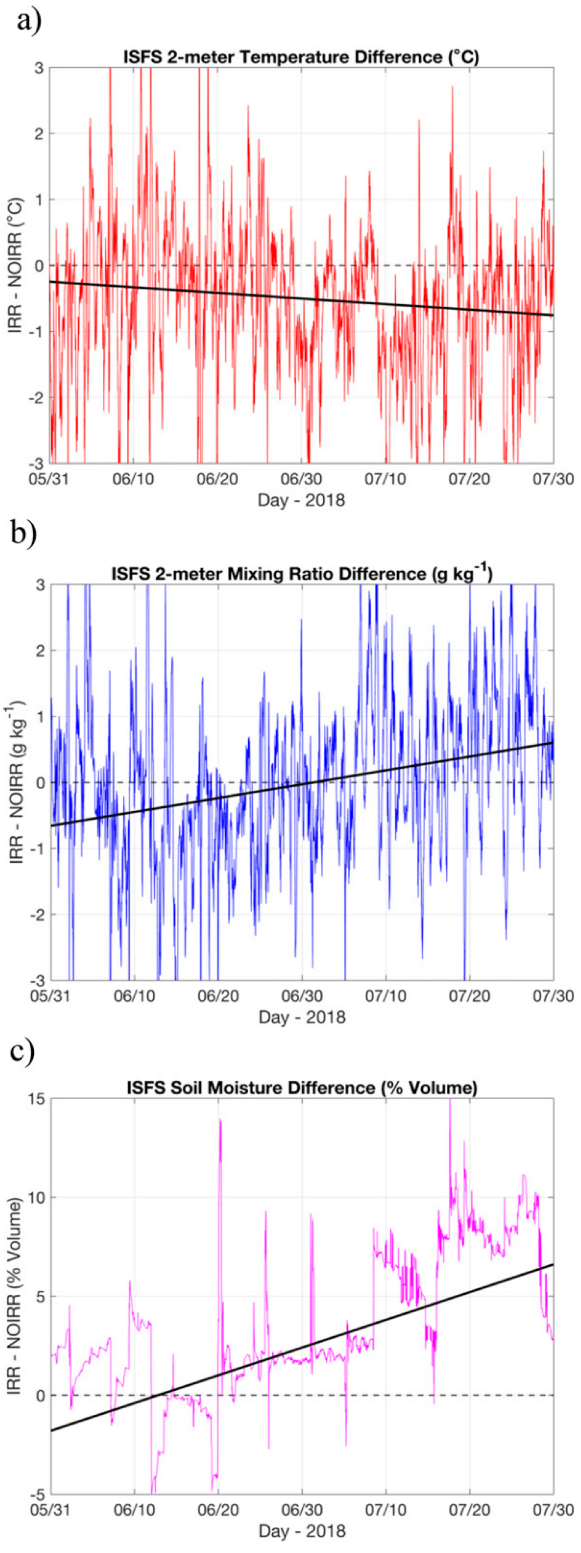

FIG. 2. Difference in ISFS 5-min quantities averaged over irrigated and nonirrigated sites: (a) 2-m air temperature (°C), (b) 2-m mixing ratio (g kg^{-1}), and (c) 5-cm soil moisture (%volume). The dashed black line represents no difference while the solid black line represents a statistically significant (at 99% level) linear fit.

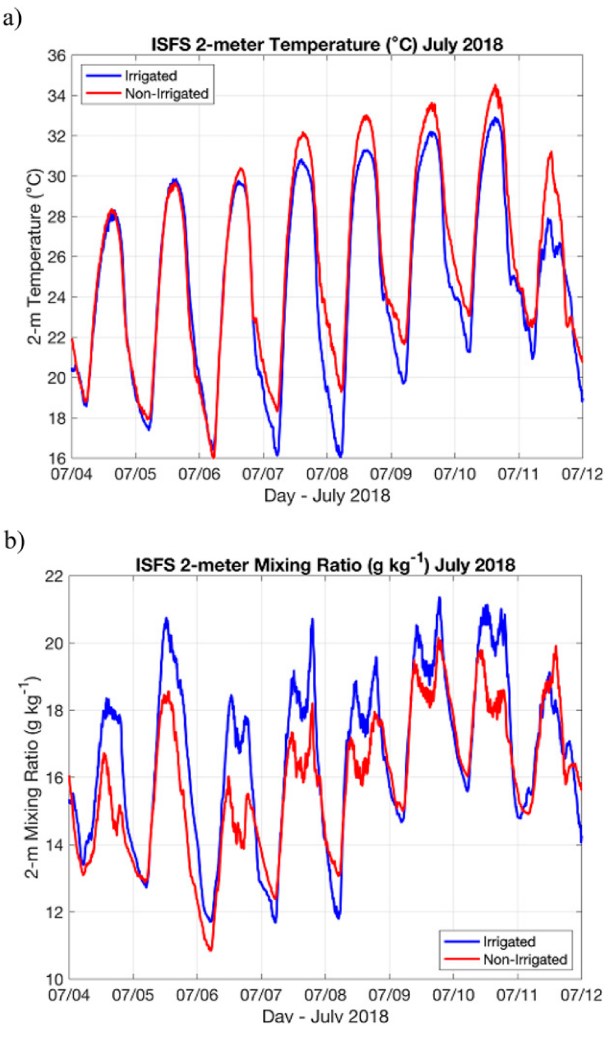

FIG. 3. Pre-IOP2 near-surface meteorology averaged over irrigated (blue) and nonirrigated (red) ISFS sites for (a) 2-m air temperature (°C) and (b) 2-m mixing ratio (g kg^{-1}).

and the 5%–10% higher volumetric soil moisture over irrigation.

Figures 3a and 3b display the near-surface meteorology during a period of both irrigation and strong L–A interactions. The period of 4–11 July was 5 days prior to IOP2, during which time both irrigation applications and precipitation were observed. Sustained warming (Fig. 3a) and moistening (Fig. 3b) were observed over both IRR and NOIRR locations. The higher sensible heat flux (Q_h) over NOIRR locations led to an average 4°C increase in temperature for 6–10 July compared to 2.5°C over the IRR locations. The 2-m mixing ratio over this same 4-day period show dual peaks, one in the late morning and one in the late afternoon. The morning peak is associated with rapid boundary layer growth prior to drying from the onset of entrainment from the free atmosphere, while the afternoon peak is associated with moisture flux convergence during the afternoon–evening transition to a stable surface layer (further discussion is provided in section 3).

The present study examines the diurnal cycle on 24 July 2018 in the middle of IOP2 when irrigation was widespread throughout the western half of the GRAINEX study region. This day is selected because of dry conditions, accompanied by a relatively clear sky with light winds that presented suitable conditions for L–A interactions. In other words, influence of large-scale active synoptic forcing was absent and the land's influence on L–A interactions can be discernable.

c. *Land surface and atmospheric modeling*

The WRF Model version 4.2 (Skamarock et al. 2019) was utilized to simulate atmospheric evolution for the period from 2100 UTC (1500 LST) 23 July 2018 to 0600 UTC (0000 LST) 25 July 2018. The analysis presented will focus on the time period starting at 0600 UTC 24 July 2018 (0000 LST 24 July) and ending at 0600 UTC 25 July (0000 LST 25 July). The model spinup period was prior to 0600 UTC 24 July, allowing for dynamic adjustment of the modeled fields, and is excluded from the analysis. The size of the domain is 1000 km × 1000 km with 1-km resolution and centered between Lincoln and York (40.797°N, 97.001°W) (Fig. 1c). Initial and boundary conditions are supplied by the High-Resolution Rapid Refresh (HRRR; Benjamin et al. 2016) analyses. HRRR was chosen for its hourly assimilation of conventional observations using Gridpoint Statistical Interpolation (Wu et al. 2002; Whitaker et al. 2008; Kleist et al. 2009), 15-min radar data assimilated every 15 min over the hour assimilation window, and the 3-km grid spacing of the operational model is of the same order of magnitude as the simulations presented here that used 1-km grid spacing. To further maintain consistency between the WRF hindcasts and the operational HRRR forecasts, matching physics packages were employed, including RRTMG longwave and shortwave radiation (Iacono et al. 2008), Thompson Microphysics (Thompson et al. 2008), and Mellor–Yamada–Nakanishi–Niino (MYNN) PBL (Nakanishi and Niino 2006, 2009) parameterizations. A key difference between HRRR analyses and the WRF simulation, and particularly relevant to L–A interaction studies is the utilization of two different land surface models (LSMs). Whereas the operational model uses the RUC LSM (Benjamin et al. 2016), the simulations here utilized the Noah LSM (Tewari et al. 2004). It is selected because of its ability to reliably represent land surface processes and L–A interactions. In the past, the authors of this paper and others have successfully applied Noah LSM to various L–A interactions studies (e.g., Hong et al. 2009; Li et al. 2018; Mahmood et al. 2020; Nair et al. 2019; Rodgers et al. 2018; Winchester et al. 2017).

WRF simulation output was every 15 min while the observational dataset was upscaled from 5- to 15-min output to match the WRF output and capture a broader temporal scale of turbulent eddies. The 1-km grid spacing is coarse and in the turbulence gray zone, or "terra incognita" (Wyngaard 2004), but the largest PBL eddies are being resolved and as such may be double counted in terms of boundary layer diffusivity. In addition, the vertical grid spacing was ~7 m in the lowest 25 m, ~20 m in the remainder of the surface layer, ~60 m through the top of the boundary layer (1–1.25 km), and ~125 m and stretched to 500 m in the stratosphere, up to 25 km.

To provide the land surface initial condition and lower boundary forcing, the National Aeronautics and Space Agency (NASA) Land Information System (LIS) version 7.2 (Kumar et al. 2006; Peters-Lidard et al. 2007) was utilized. LIS is a flexible land surface modeling and data assimilation framework developed with the goal to integrate satellite- and ground-based observational data products and advanced land surface modeling techniques to produce optimal fields of land surface states and fluxes and may be run offline or coupled. For the purposes presented here, LIS was run offline and the resultant land surface state used to replace the HRRR analysis land surface initial and boundary conditions. The National Land Data Assimilation System phase 2 (NLDAS2) (Cosgrove et al. 2003) was used for meteorological forcing of the offline LSM simulation. NLDAS2 is derived from the North American Regional Reanalysis (NARR; Mesinger et al. 2006) at 0.125° grid spacing with a 3-h temporal spacing. In addition to increased resolution, NLDAS2 uses precipitation data assimilation to produce a significantly improved product compared to other NCEP reanalyses (Kennedy et al. 2011).

To provide best estimates of initial land surface state, LIS was run offline from May of 2015 through model initialization time utilizing LIS ensemble Kalman filter data assimilation of Soil Moisture Active Passive (SMAP; O'Neill et al. 2020) satellite retrievals. Soil moisture retrievals utilized are from the SMAP L3 enhanced soil moisture product, based on the 33-km retrieval algorithm but after oversampling the SMAP footprint, is output at 9-km spatial resolution.

In the results presented here, LIS was run with SMAP data assimilation using a 1D ensemble Kalman filter with 12 ensemble members. Further, the SMAP retrievals were debiased using cumulative distribution functions (cdf) of the satellite data. Subsequently, in the WRF simulations, the soil moisture fields were initialized using data from the offline runs of LIS. These LIS soil-moisture-forced WRF simulations will be referred from here on as WRF_NLDAS2. The temporal evolution of surface volumetric soil moisture averaged for the IRR and NONIRR site locations (Fig. 4) in WRF_NLDAS2 show similar trends compared to corresponding averaged observations. Similar to observations, average soil moisture for the irrigated sites in WRF_NLDAS2 is higher compared to nonirrigated sites. However, the simulated difference between the irrigated and nonirrigated sites is substantially smaller compared to the observations (Fig. 4a). Further, soil moisture in WRF_NLDAS2 is an underestimate for the irrigated sites and overestimate for the nonirrigated sites. Despite these differences, comparison to HRRR soil moisture fields shows that our estimates using the NLDAS2 forced LIS offline simulations substantially improve spatial gradients, except in the vicinity of site 6 (Fig. 4b). However, this is due to site 6 being located along the Big Blue River with the strongest irrigation–nonirrigation gradient (Fig. 1a).

Despite the above-described differences, when compared to observations, WRF_NLDAS2 exhibits qualitatively similar responses of surface energy budget and meteorology to variability in soil moisture (Figs. 5a,b). However, note that WRF_NLDAS2 under and overestimated latent and sensible heat fluxes (Fig. 5b), respectively, compared to observations. Additional comparison of data from ISFS, ISS, and WRF_NLDAS2 is provided in Table 1.

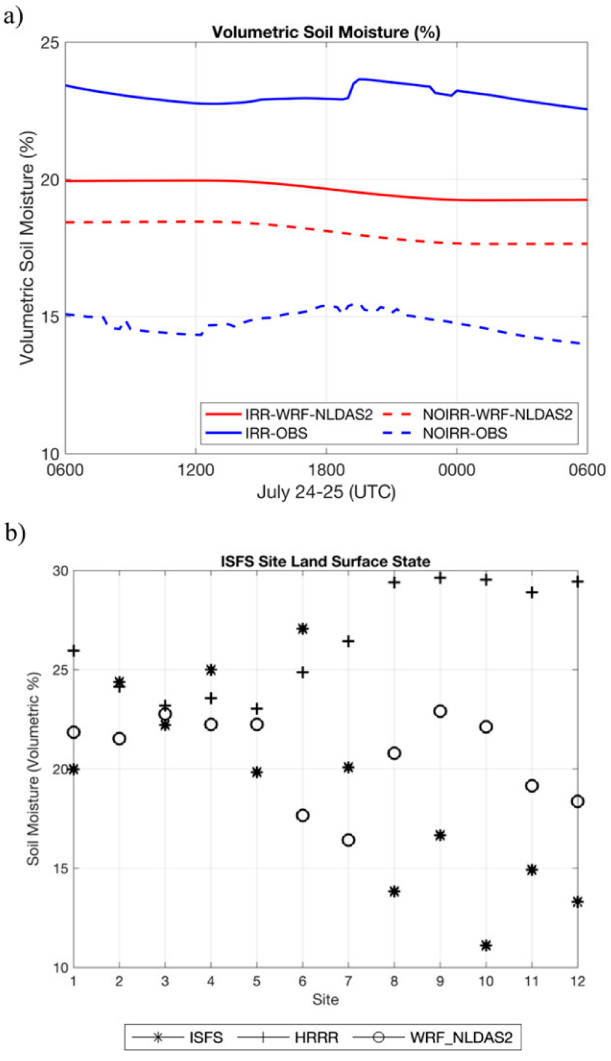

FIG. 4. Volumetric soil moisture on 24 Jul 2018: (a) observed and simulated soil moisture of irrigated (IRR) and nonirrigated (NOIRR) areas; observations are from the ISFS and averaged over irrigated (solid) and nonirrigated areas (dashed), and (b) average site specific volumetric soil moisture for ISFS observations (*), HRRR analyses (+), and WRF_NLDAS2 (o). Sites 1–6 are over IRR, and sites 7–12 are over NOIRR. LST = UTC − 6 h.

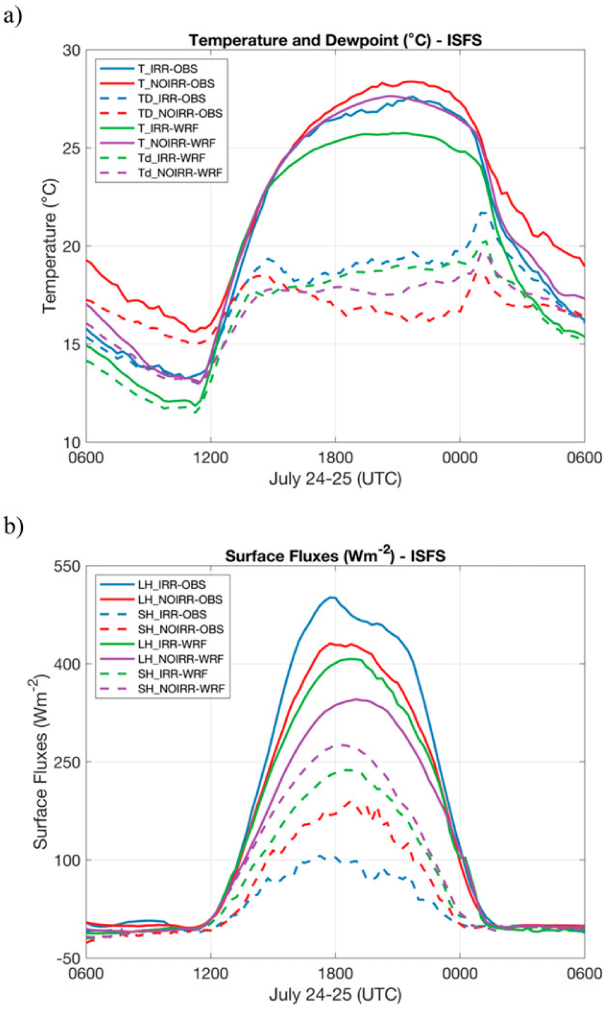

FIG. 5. Spatially averaged (a) air temperature and dewpoint temperature and (b) latent heat and sensible heat fluxes over irrigated and nonirrigated areas for the ISFS sites and WRF_NLDAS2 simulations.

The modeled evolution of surface energy fluxes, meteorology and planetary boundary layer are generally comparable to observations. This provides confidence in the utilization of the WRF_NLDAS2 to analyze the impacts of irrigation on atmospheric evolution. However, note that the magnitude of differences may be underestimated by WRF_NLDAS2.

3. Observed planetary boundary layer evolution over irrigated and nonirrigated land uses

Time evolution of near-surface thermodynamic variables and wind at the York (IRR) and Rogers Farm (NOIRR) are examined using bihourly radiosonde observations, roughly at 5-m elevation. Note that since radiosonde observations are utilized, the time series duration is from 1100 UTC 24 July (0500 LST 24 July) to 0100 UTC 25 July (1900 LST 24 July) (Figs. 6a–c). The PBL height (PBLH) is estimated from radiosonde observations based on the vertical variation of the bulk Richardson number. This methodology has been validated by comparison to estimates derived using the signal-to-noise ratio from coincident wind profiler observations (Rappin et al. 2021).

a. *Observed temperature and dewpoint temperature*

The air and dewpoint temperature from ISS soundings for IRR and NOIRR ISS sites (Fig. 6a) were compared to observations from the ISFS locations (Fig. 5a) and similar differences in diurnal evolution were found. The time where the IRR and NOIRR temperatures begin to separate (Fig. 6a) are consistent as is the timing of maximum temperature (~26°–27°C) achieved over both land uses (~2100–2300 UTC, ~1500–1700 LST). The dewpoint temperature differences are more pronounced but still qualitatively similar between locations. While the temporal

TABLE 1. Averaged observations from six irrigated (IRR) and six nonirrigated (NOIRR) ISFS sites, York (IRR) and Rogers Farm (NOIRR) ISS sites, and the WRF_NLDAS2 simulations. Radiosondes were launched bihourly only from the ISS sites and hence PBLH is available for these two sites and WRF_NLDAS2. Heat flux measurements were from the ISFS sites and WRF_NLDAS2.

Date and time	IRR/NOIRR						
24–25 Jul	T (°C)	Td (°C)	WSPD (m s^{-1})	VPD (hPa)	Q_h (W m^{-2})	Q_e (W m^{-2})	PBLH (m)
0900 UTC							
ISFS	13.8/16.8	13.7/15.8	1.58/2.47	0.1/1.2	−7/−19	13/−6	—
ISS	14.2/13.9	13.8/13.5	0.74/0.32	0.4/0.4	—	—	—
WRF	12.5/13.9	12.1/13.7	3.57/2.36	0.6/0.5	−9/−7	−7/−9	18/52
1000 UTC							
ISFS	13.5/16.4	13.5/15.4	1.92/2.26	0.1/1.2	−5/−12	−3/−2	—
ISS	14.1/13.4	13.7/13.1	0.66/0.41	0.5/0.3	—	—	—
WRF	12.1/13.4	11.8/13.2	3.16/2.19	0.5/0.2	−5/−8	−4/−8	15/20
1100 UTC							
ISFS	13.3/15.7	13.3/15.0	2.30/2.19	0.0/0.7	−10/−9	−5/−3	—
ISS	13.9/13.0	13.5/12.7	0.86/0.55	0.5/0.3	—	—	—
WRF	12.1/13.4	11.7/13.2	2.45/2.30	0.3/0.1	−7/−6	−5/−5	12/24
1200 UTC							
ISFS	14.2/16.0	14.2/15.4	1.71/1.96	0.0/0.8	−5/−8	−2/−1	—
ISS	14.3/13.5	13.7/13.0	0.75/0.26	0.6/0.4	—	—	—
WRF	13.7/14.4	13.1/13.8	2.50/2.12	0.3/0.1	3/10	8/9	11/22
1300 UTC							
ISFS	17.3/18.4	16.8/17.2	1.77/1.86	0.7/1.6	8/11	58/59	NA
ISS	14.3/18.3	16.0/16.6	0.90/0.12	1.6/2.3	NA	NA	36/85
WRF	18.3/18.1	15.9/15.6	2.68/2.05	0.6/0.7	39/57	76/61	45/52
1400 UTC							
ISFS	20.7/21.0	18.6/18.4	1.18/1.94	3.0/3.7	34/49	150/130	—
ISS	20.7/20.5	17.9/17.0	1.04/2.0	4.0/4.7	—	—	—
WRF	21.3/21.3	17.7/17.2	1.17/1.79	3.0/3.1	90/117	153/125	85/111
1500 UTC							
ISFS	23.4/23.6	19.2/18.2	1.14/2.29	6.6/8.1	64/97	280/266	NA
ISS	23.0/22.6	18.4/17.5	0.90/1.93	7.0/7.5	—	—	165/235
WRF	23.3/23.6	17.6/17.8	1.23/1.51	5.0/5.7	132/173	245/195	184/202
1600 UTC							
ISFS	25.0/25.1	18.2/17.9	1.24/2.24	10.7/11.4	77/124	395/343	—
ISS	24.7/24.3	17.4/17.8	1.05/2.13	11.0/10.2	—	—	—
WRF	24.2/25.0	17.9/17.7	1.18/1.43	8.4/8.6	179/218	317/261	394/384
1700 UTC							
ISFS	25.9/26.3	18.4/17.4	1.41/3.14	12.1/14.3	91/153	474/430	—
ISS	25.2/25.7	17.3/16.8	1.43/2.68	12.4/13.9	—	—	801/943
WRF	24.9/26.0	18.0/17.6	0.54/1.58	9.7/11.5	210/254	371/310	606/642
1800 UTC							
ISFS	26.5/27.1	18.6/16.8	1.93/3.13	13.1/16.7	98/169	475/464	—
ISS	25.4/26.7	17.1/16.8	1.10/2.70	13.0/16.0	—	—	—
WRF	25.3/26.7	18.3/17.9	0.69/1.54	10.9/13.4	233/276	401/337	821/928
1900 UTC							
ISFS	26.8/27.7	19.1/16.8	1.72/2.96	13.1/18.0	91/168	510/414	NA
ISS	26.1/27.0	16.8/16.2	1.46/2.51	14.8/17.3	—	—	972/1253
WRF	25.6/27.2	18.7/17.7	0.82/1.64	11.2/14.5	236/271	407/346	990/1245

TABLE 1. (*Continued*)

Date and time	IRR/NOIRR						
24–25 Jul	T (°C)	Td (°C)	WSPD (m s^{-1})	VPD (hPa)	Q_h (W m^{-2})	Q_e (W m^{-2})	PBLH (m)
2000 UTC							
ISFS	26.8/28.1	19.1/16.6	1.47/2.59	13.2/19.2	60/159	389/419	—
ISS	26.4/27.4	17.6/16.3	1.34/2.69	14.3/18.0	—	—	—
WRF	25.7/27.5	19.0/17.5	1.03/1.57	11.3/15.7	209/242	377/336	1159/1345
2100 UTC							
ISFS	27.4/28.2	19.3/16.6	1.27/2.18	14.1/19.4	72/107	479/335	—
ISS	26.9/27.6	17.4/15.8	1.11/1.90	15.5/19.0	—	—	1068/1082
WRF	25.7/27.6	19.0/17.6	0.76/2.04	11.4/16.7	175/194	338/305	1215/1375
2200 UTC							
ISFS	27.4/28.3	19.4/16.5	1.66/1.99	14.0/19.8	38/92	325/313	—
ISS	27.1/28.3	18.3/15.1	1.39/1.63	14.9/21.4	—	—	—
	25.7/27.4	19.0/18.0	1.06/2.59	11.1/16.8	129/150	285/257	1194/1412
2300 UTC							
ISFS	27.2/28.1	19.2/16.5	1.15/1.98	13.9/19.2	23/44	264/229	—
ISS	27.4/28.3	17.7/15.5	1.35/1.69	16.3/20.7	—	—	934/1036
WRF	25.4/27.0	18.8/18.2	1.17/2.50	11.0/15.9	75/82	219/192	1158/1362
0000 UTC							
ISFS	26.6/27.3	19.7/16.6	0.94/1.45	11.8/17.4	3/6	155/106	—
ISS	27.4/28.0	17.8/15.4	1.05/0.98	16.0/20.3	—	—	—
WRF	24.8/26.4	19.2/18.5	0.75/2.71	10.7/14.8	14/19	103/113	1058/1252
0100 UTC							
ISFS	24.5/25.5	21.7/18.4	1.12/1.36	4.9/11.4	−2/−4	14/13	—
ISS	26.2/26.2	18.6/18.1	1.05/0.43	12.6/13.3	—	—	—
WRF	24.0/25.2	20.1/19.6	0.92/1.86	9.1/13.2	−1/−5	12/20	863/1112
0200 UTC							
ISFS	20.9/22.7	20.0/17.4	1.17/1.22	1.4/7.7	−3/−1	3/1	—
ISS	23.9/20.7	18.6/18.8	0.98/0.44	8.3/2.7	—	—	—
WRF	20.1/21.3	18.3/18.3	0.85/1.44	6.4/9.1	−3/−7	−5/−2	647/899
0300 UTC							
ISFS	19.4/21.6	18.9/16.9	1.04/1.33	0.8/6.7	0/−2	0/0	—
ISS	23.2/18.3	18.6/17.2	0.74/0.41	7.0/1.3	—	—	—
WRF	17.9/19.9	17.6/17.6	1.29/1.79	2.5/4.2	−4/−2	−7/−2	334/246

resolution of radiosonde launch is not sufficient to capture either of the boundary layer transitions, the dewpoint temperature (~18°C) over IRR and slowly declining value over NOIRR from 1500 to 2300 UTC (mixed layer PBL phase) matched the observations at ISFS locations and provides further evidence of transitioning PBL. These similarities between ISS and spatially distributed ISFS sites provide confidence that the radiosonde observations captured atmospheric evolution satisfactorily and are characteristic of IRR and NOIRR land surface influences.

b. *Observed relative humidity and equivalent potential temperature*

When the observation of the surface evolution of thermodynamic variables (Figs. 6a–c) are evaluated along with corresponding vertical profiles of mixing ratio (q) and potential temperature (θ) (Figs. 7a–d), a more complete picture of the diurnal evolution of the PBL emerges. The relative humidity evolution is similar to that of the dewpoint temperature, though opposite in trend early in the day, due to the rapidly increasing temperature. The monotonic decreases in relative humidity until 1700 UTC (1100 LST) is associated with rapid growth of the PBL and entrainment drying at both irrigated and nonirrigated regions (Fig. 6b). After 1700 UTC, relative humidity shows relatively small changes compared to earlier hours of the day. The θ_e evolution shows very rapid increases over both land uses and is in step with the air temperature and dewpoint temperature just after the morning transition. By 1700 UTC (1100 LST) θ_e reached to about 335 K (Fig. 6b) over Rogers Farm (NOIRR) as the air

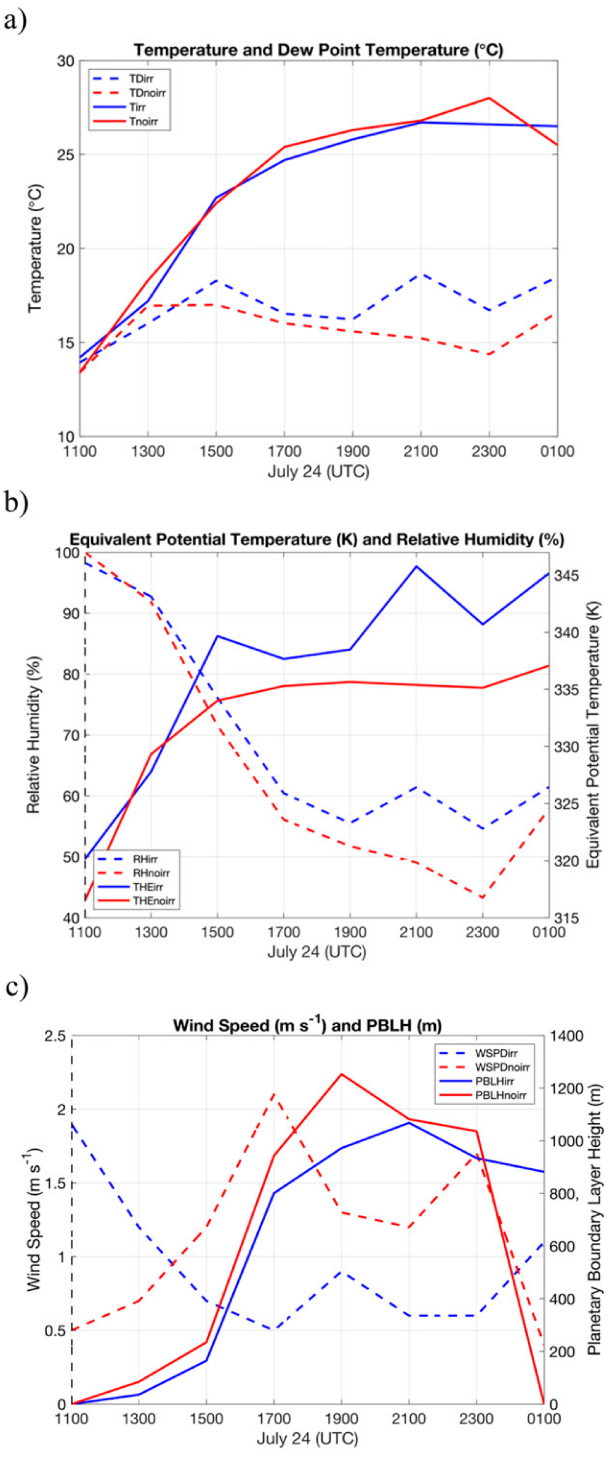

FIG. 6. Near-surface sounding observations from the ISS sites at York (IRR) and Rogers Farm (NOIRR): (a) air temperature and dewpoint temperature, (b) equivalent potential temperature and relative humidity, and (c) wind speed and planetary boundary layer height.

temperature (dewpoint temperature) increases (decreases) slowly until the afternoon–evening transition begins. At York (IRR), θ_e increase was comparable to Rogers Farm (NOIRR) in the earlier part of the morning but subsequently started to increase at a faster pace around 1400 UTC (0800 LST). This is also in step with changes in air and dewpoint temperature. The PBLH shows a midafternoon maximum about 100–150 m higher over Rogers Farm (NOIRR) (Fig. 6c), consistent with the larger Q_h at that location. Taken together with the higher θ_e and Q_e at York (IRR), it is reasonable to conclude a higher column integrated moist static energy exists over irrigation compared to NOIRR cropland. Compared to York (IRR), Rogers Farm (NOIRR) observed higher wind speeds during most of the day and higher midafternoon maximum wind speeds as well (Fig. 6c). Similar observations are also made over the ISFS sites. We suggest that relatively larger Q_h over NOIRR and the associated Q_h gradient between IRR and NOIRR played a role in these differences in wind speeds (Fig. 2 in the supplemental material).

c. *Entrainment from the free atmosphere to PBL and its evolution*

The vertical soundings of θ and q through the depth of the PBL and up into the free atmosphere allow for diagnosis of entrainment into the PBL from the free atmosphere and the feedback on surface and mean PBL fields. Comparing the 2-hourly radiosonde observations from 1100 UTC 24 July (0500 LST) to 0100 UTC 25 July (1900 LST 24 July), at York (IRR) and Rogers Farm (NOIRR) (Figs. 7a,b), it is evident that there are noticeable differences in the evolution of the convective mixed layer. Both York (IRR) and Rogers Farm (NOIRR) display strong nocturnal surface inversions, with York (IRR) displaying weak stability through a poorly mixed residual layer extending up to roughly 1.25 km at sunrise (Figs. 7a,c). While Rogers Farm (NOIRR) on the other hand does show a well-mixed residual layer extending from the top of the surface inversion to 1 km (Figs. 7b,d). Note that at York (IRR) and Rogers Farm (NOIRR) there is a weak capping inversion observed at 600 and 800 m, respectively, at sunrise. Both weak inversions are well observed in the mixing ratio profiles (Figs. 7c,d) and are quickly eroded by the next sounding time (1300 UTC).

A very rapid increase in temperature occurs at both IRR and NOIRR locations from sunrise to late morning (1100–1700 UTC; 0900–1100 LST) while dewpoint temperature also increases quickly from sunrise to midmorning (1100–1500 UTC; 0500–0900 LST). These results are similar to the findings by Van Heerwaarden et al. (2009), where an idealized examination of the impact of entrainment on surface fields and PBL development was discussed. The period from sunrise to midmorning local time corresponds to strong surface radiative forcing prior to feedbacks from PBL growth and entrainment. Between 1300 and 1700 UTC (0700 and 1100 LST), the boundary layer grows rapidly and free atmospheric entrainment is significant. The growth is observed in the increasing depth of the residual, slightly stable (neutral) mixed layer over York (IRR) (Rogers Farm, NOIRR), maximizing at

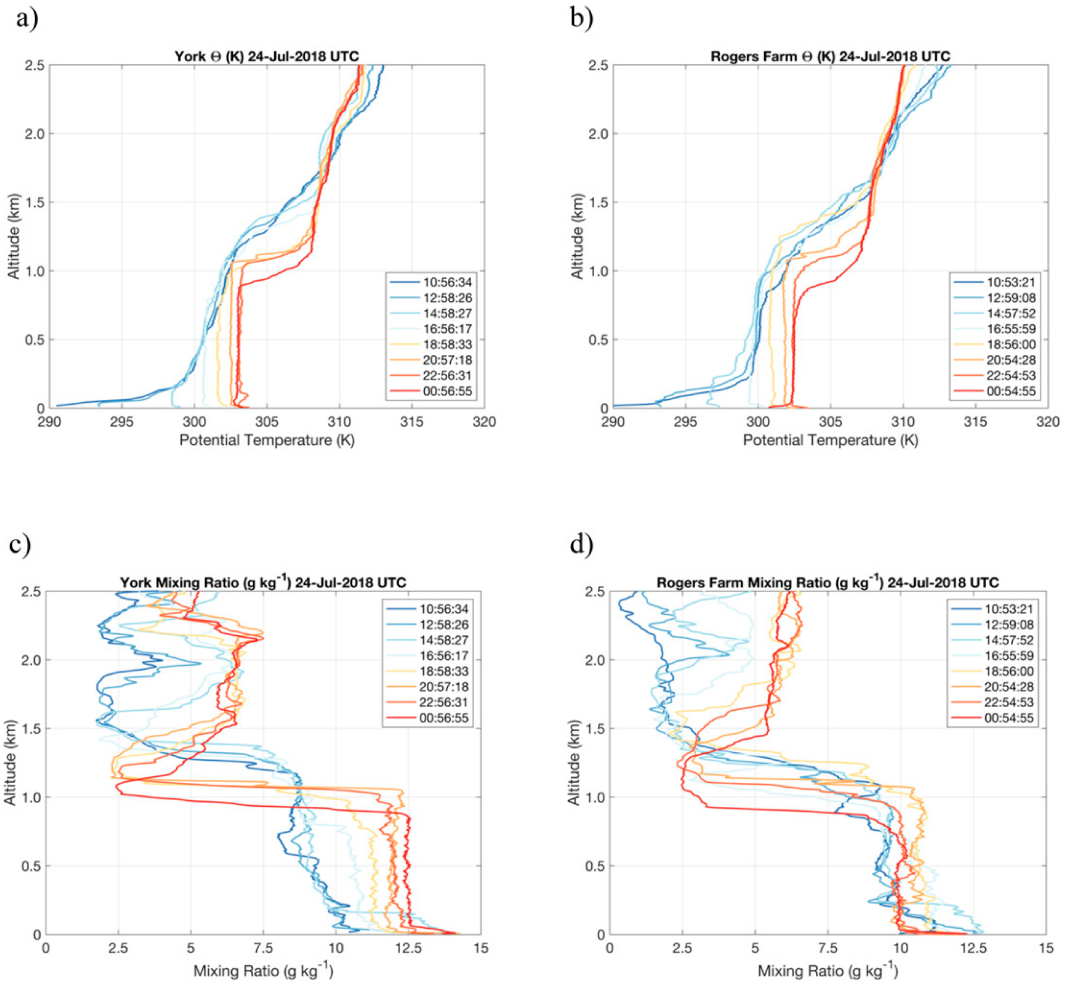

FIG. 7. (a),(b) Boundary layer and lower free atmosphere θ; (c),(d) boundary layer and lower free atmosphere mixing ratio for 24 Jul 2018. Times are in UTC. (Modified from Rappin et al. 2021.)

the 1500 UTC (0900 LST) sounding and in the sharpening of the moisture gradient during this time.

The higher temporal resolution at the ISFS locations permits the observance of the morning peak in dewpoint temperature (~19°C) and its rapid decline due to entrainment drying and its correspondence to the peak growth in PBLH (Van Heerwaarden et al. 2009). The drying impacts the PBL quite differently between IRR and NOIRR cropland as observed at the ISFS sites (Fig. 5a). By 1700 UTC (1100 LST), the near-surface moisture content over IRR has begun to steadily increase which is reflected in increasing dewpoint temperature. Conversely, the observed moisture content over NOIRR locations declined quite rapidly once entrainment commenced and is reflected in lowering of the dewpoint temperature, which continued through the remainder of the daylight hours until the afternoon–evening transition.

The impact of dry air entrainment is also observable when considering the evolution of dewpoint temperature and its modulation by surface fluxes (Figs. 5a,b). As observed in the spatially averaged surface fluxes (Fig. 5b), both Q_e and Q_h rates of increase begin to separate after 1500 UTC (0900 LST), during the period of most rapid growth of the PBL and hence, entrainment. As dry air is entrained from the free atmosphere, the vapor pressure deficit (VPD) (Table 1) at both locations increases after a rapid decline due to the strong radiative forcing that commences after sunset. As a result, continued strong latent heating occurs and is particularly noticeable over NOIRR croplands. The increased VPD favors continued large Q_e across the GRAINEX domain, but the lower soil moisture content of NOIRR cropland limits Q_e as observed in differences in its increase (Fig. 5b).

During the pre and early growth phase (~1100–1500 UTC; 0500–0900 LST), the surface layer is heated and moistened by increasing downwelling shortwave radiation over the GRAINEX domain. The increase in temperature and dewpoint temperature is constrained to the lowest layer due to the strong stability of the nocturnal inversion. Around 1500 UTC (0900 LST), at the conclusion of the morning dewpoint temperature peak, the surface layer has eroded the nocturnal inversion and mixed growth commenced. By 1700 UTC

(1100 LST), the top of the mixed layer has reached 800 and 900 m over IRR and NOIRR, respectively (Figs. 7a–d). Note that during this period over IRR, the deepening mixed layer is also moistening while over NOIRR, the area above the nocturnal inversion moistens. IRR is supported by a larger increase in Q_e from the surface leading to larger moistening from below and smaller Q_h from the surface leading to less dry air entrainment from above (due to lack of turbulent mixing). The larger Bowen ratio over NOIRR shows that with limited moistening from the surface, development of the mixed layer conserves the boundary layer mixing ratio leading to its redistribution in the vertical as opposed to deep moistening observed over IRR.

Between IRR and NOIRR, the ending of mixed layer growth through and during the mature phase of its evolution from late morning to late afternoon [1700–2300 UTC (1100–1700 LST)], is as equally varied as during the growth phase. Between 1700 and 1900 UTC (1100 and 1300 LST), the soundings over IRR show that the top of the mixed layer has reached its peak altitude in terms of θ and q. Entrainment drying is compensated by increasing Q_e, resulting in the establishment of an equilibrium mixed layer altitude from 1900 to 2300 UTC (1300 and 1700 LST). Conversely, over NOIRR, the large Q_h rate supports continued growth of the mixed layer through 1900 UTC (1300 LST), at which point q is mixed through the depth of the PBL (Fig. 7d). Between the 1900 and 2100 UTC (1300 and 1500 LST) sounding, the smaller Q_e (relative to IRR), leads to drying below 250 m over NOIRR while the PBL remains well mixed and warm. In the final hours of the day, the well-mixed boundary layer continues to warm, though at a greatly reduced rate due to the rapid decline of turbulent heat flux. With the rapid lowering of Q_h, the PBLH also falls quickly. The decline is much more pronounced over NOIRR (Figs. 7b,d), where it falls by 400 m during the 6-h period leading to sunset. In contrast, over IRR the mixed layer falls by just half that height and is constrained to just the 2 h prior to sunset during the afternoon–evening transition. Also note that the surface layer superadiabatic lapse has dissipated by the sunset sounding at 0100 UTC 25 July (1900 LST 24 July) over NOIRR, but not at the IRR location as found in the spatially averaged ISFS locations.

4. Simulation of planetary boundary layer evolution over irrigated and nonirrigated land uses

Numerical model simulations with realistic soil moisture spatial distributions are used to examine if the pattern of differences in atmospheric evolution holds when statistics of larger populations of irrigated and nonirrigated locations are considered. Also, since numerical model simulation considers a wider range of irrigation fraction (IF) and soil moisture conditions than those sampled by observational sites, it allows for systematic analysis of atmospheric evolution as a function of such land surface variability. Figures 8a–e conceptualize the effect of this variability utilizing WRF_NLDAS2 simulations, where time evolution of surface meteorology, energy fluxes, and boundary layer evolution vary as a function of IF. The domain considered for the analysis is shown in Fig. 1c (Salmon et al. 2015) with the Ozdogan and Gutman (2008) irrigation fraction utilized (Fig. 1a).

a. *Sensible heat flux*

In the WRF_NLDAS2, the Q_h evolution resembles that of a "normal distribution," with a peak in flux during the peak in net incident solar radiation (not shown) around 1900 UTC (1300 LST) (Fig. 8a). It suggests that the larger the irrigation fraction, the larger the moisture content of the soil–vegetation system which leads to a smaller Bowen ratio with much of the incident radiation used for evaporation. As a result, there is a larger spread in maximum Q_h in WRF_NLDAS2 due not only to the more realistic magnitude of soil moisture over the GRAINEX region, but also a higher soil moisture content with irrigation. Overall, simulations suggest that higher IF (~60%) results in lower Q_h (at peak, it is ~275 W m^{-2}) and is consistent with our understanding.

b. *Air temperature*

The WRF_NLDAS2 air temperature (Fig. 8b), like Q_h, displays a noticeable separation between the temperature evolution of the two largest and smallest IF [IF $\geq$ ($<$) 37.1%]. As a result of the reduced Bowen ratio over IRR cropland, there is a strong negative correlation between IF and daytime maximum temperature. Despite this difference, the simulation yielded a similar diurnal amplitude as the nocturnal temperature minimum is also negatively correlated with IF. The wetter IRR soils have a higher heat capacity, and therefore higher thermal inertia than the NOIRR cropland thereby limiting its daily maximum temperature. Conversely, the NOIRR region of the GRAINEX domain would be expected to cool more rapidly in the absence of moisture effects.

The relative extent of the irrigation fraction across the croplands impacts the soil moisture throughout the GRAINEX domain, which in turn leads to the differences in maximum temperature. WRF_NLDAS2 shows a spread in maximum temperature to accompany the larger spread observed in Q_h, with irrigation fraction. As noted in the previous section, the WRF_NLDAS2 simulation yields the largest temperature deviations from observations just prior to the two transition periods, suggesting again that the deviations in the diurnal maximum temperature and associated stronger wind speeds lead to a slower decay of the upward heat flux and the diurnal minimum temperature value.

c. *Latent heat flux*

As expected, Q_e is higher (up to ~365 W m^{-2}) with higher IF (~60%) and like Q_h, the evolution of Q_e resembles that of a normal distribution, with a peak in fluxes during the peak in net incident radiation around 1900 UTC (1300 LST) (Fig. 8c). WRF_NLDAS2 has a smaller magnitude Q_e and is more aligned with the soil moisture variations across the various IF quartiles. The reduction of Q_e, much like that of Q_h, is rapid once the buoyancy flux declines. However, this the reduction is not uniform with irrigation fraction. The higher IF, by virtue of its large soil–vegetation moisture, continues evapotranspiration at a greater rate than lower IF, leading to higher near-surface moisture content.

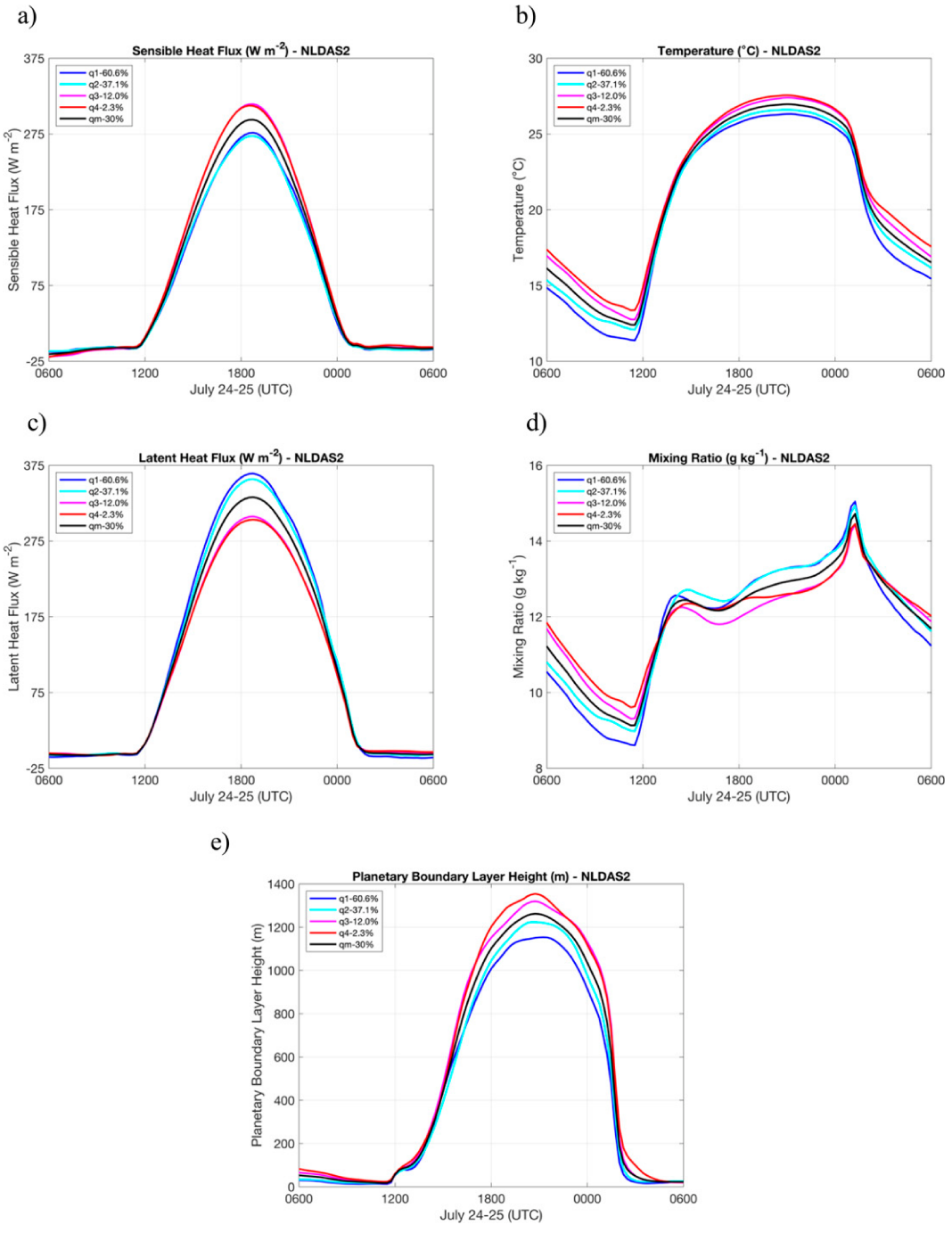

FIG. 8. WRF_NLDAS2 simulations for various levels of irrigation fractions and diurnal evolution for (a) sensible heat flux, (b) temperature, (c) latent heat flux, (d) mixing ratio, and (e) planetary boundary layer height. The irrigation fractions of 2.3% (red), 12.0% (magenta), 37.1% (cyan), and 60.6% (blue) are calculated for are shown in Fig. 1b. The black curve represents mean.

d. Mixing ratio

The early morning hours (midnight local time to sunrise) are characterized by a lowering of the 2-m q that is commensurate with the lowering of 2-m temperature (Fig. 8d). Rappin et al. (2021) show that over IRR cropland, near saturation conditions occur and dew formation may aid in water vapor depletion. The moisture evolution leading up to afternoon–evening transition is governed by soil moisture and evapotranspiration. There is an increase in the mixing ratio during

the early, radiatively weakly forced period of the morning transition at a rate proportional to the irrigation fraction. While entrainment of residual or free tropospheric air from the boundary layer is still thin, the rapid rise in moisture flux associated with the rapid increase in buoyancy flux leads to a spike in the 2-m q that becomes diluted as boundary layer entrainment warms and lifts the convective mixed layer.

Around 1300 UTC (0700 LST), or approximately 2 h after sunrise, q has a nearly uniform mean value across the domain (~12–12.5 g kg^{-1}), and subsequently lowers slightly as the PBLH reaches its most rapid growth rate between 1400 and 1700 UTC. The lowering in moisture content is likely associated with strong dry air entrainment as the mixed layer grows rapidly and concludes once evapotranspiration, as measured by Q_e, closes in on its peak diurnal value.

After morning hours and when the convective mixed layer is nearing its maximum height above ground layer, an approximate equilibrium occurs between the positive moisture flux from the lower boundary and a negative moisture flux from the top boundary (e.g., dry air entrainment). As found in the observations, the significant difference in lower boundary moisture and resultant differences in lower-surface layer buoyancy flux leads to differences in PBL thickness (Figs. 8a,e) between IRR and NOIRR cropland and subsequently IRR (NOIRR) sites tend to see a slight increase (decrease) in mixing prior to the evening transition (Figs. 6 and 7). However, the simulations show a tendency for a slight increase during the equilibrium (not shown). While this certainly can be attributed to the soil moisture initial condition, PBL parameterizations are likely a contributing factor but beyond the scope of the current objectives.

The afternoon–evening transition is characterized by a rapid spike in near-surface water vapor as clearly observed in the GRAINEX data, and the WRF_NLDAS2 simulation. The spike is the result of the interplay between continued surface moisture fluxes and turbulent flux divergence associated with the weakening vertical temperature brought on by the loss of turbulent heat flux and direct radiational cooling of the boundary layer. In WRF_NLDAS2, where the initial soil–crop moisture distribution more accurately reflects observations, the magnitude of the moisture spike increases as the irrigation fraction increases.

e. *Planetary boundary layer height*

Overall PBLH is lower for the higher IF and the higher for lower IF (Fig. 8e). Assessment of simulated data suggests that the PBLH growth commences after sunrise (1130 UTC; 0530 LST) and after the surface layer has warmed by incoming solar radiation and the turbulent heat flux has begun to increase (Fig. 8e). A pause in the simulated PBL growth occurs during the period of most rapid warming and moistening. This is the point when q has reached its morning peak (~1300 UTC; ~0700 LST). Once the mixing ratio has reached an approximate equilibrium value in the midmorning, PBL growth resumes at a rapid pace until it reaches its highest value around 2000 UTC (1400 LST). Note that the timing of maximum PBLH is consistent between WRF_NLDAS2 and the observations (Figs. 5c and 8e). The simulated PBLH exceeds that of the observed values by approximately 200 m with limited irrigated regions peaking over 1300 m and with more extensively irrigated regions reaching just under 1200 m. The overestimation of PBLH is likely associated with the overestimation of Q_h in WRF_NLDAS2 compared to observations (Fig. 5b).

5. Concluding remarks

Agriculture related land use and land cover change (LULCC) modifies land–atmosphere (L–A) interactions and evolution of the planetary boundary layer (PBL), which is further amplified when irrigation is applied. To better understand L–A interactions and PBL evolution, the Great Plains Irrigation Experiment (GRAINEX) was conducted during the growing season of 2018. This is the first campaign for this type of data collection. In this paper, we analyzed these observations to further understand the impacts of irrigation on L–A interactions and PBL evolution. In addition, we utilized the Weather Research and Forecasting (WRF) Model to further identify and quantify these impacts.

When compared to NOIRR areas, air temperatures and Q_h were lower and dewpoint temperature and Q_e were higher over IRR areas. As the day progressed, a rapid rise in the PBL and the resultant increase in PBL height (PBLH) was observed over both IRR and NOIRR locations and were associated with entrainment drying. In addition, compared to NOIRR, the PBLH remained lower by about 100–150 m over IRR. It is consistent with energy partitioning over these two land use types. Specifically, compared to NOIRR, Q_e was higher over IRR while Q_h was higher over NOIRR compared to IRR. Overall, interactions between entrainment layer drying and differences in energy partitioning over irrigated and nonirrigated areas played an important role in PBL evolution. The equivalent potential temperature (θ_e) shows rapid increases and is in step with the temperature and dewpoint temperature just after the morning transition over NOIRR. Over IRR, on the other hand, θ_e increases fairly rapidly also but at a relatively slower pace than NOIRR and is linked to a slightly slower increase in temperature and dewpoint temperature compared to NOIRR. The wind speeds also show a mid-afternoon maximum occurring over nonirrigated locations where sensible energy fluxes are higher compared to irrigated locations. In the final hours of the day with the rapid lowering of Q_h, the PBLH fell quickly. The decline was much more pronounced over NOIRR locations where it fell by ~300 m during the 6-h period leading to sunset. In contrast, over IRR the mixed layer falls by just half that height and is constrained to just the two hours prior to sunset during the afternoon–evening transition.

The WRF Model simulations reproduced and further supported these observations. In addition, the model shows, that the extent of irrigation (expressed as irrigation fraction or IF) in an area or region impacts the strength of these relationships and the magnitude of atmospheric response. For example, under ~60% IF, latent heat flux and mixing ratio reach their highest value, while air temperature and PBLH are at their lowest, and sensible heat flux is near its lowest value. On the other hand, under ~2% IF, the latent heat flux and mixing

ratio reach their lowest point while temperature, PBLH, and sensible heat flux attain their highest value.

Results from both observational and modeled data agree with our conceptual understanding of impacts of irrigation on temperature, near-surface moisture content, moist static energy (equivalent potential temperature) and PBL evolution. Findings indicate that models would benefit from explicit incorporation of irrigation (Qian et al. 2013; Van Weverberg et al. 2018; Zhang et al. 2018). Some of the common biases (e.g., warm and or dry bias) associated with model applications potentially could be linked to the absence of explicit incorporation of irrigation (Qian et al. 2020). This research also suggests that quantitative assessment of the current range of uncertainty of land–atmosphere and PBL simulations in the context of irrigation would be a useful activity in the future.

In short, the findings of this study are important because they contribute to the first assessment, that we are aware of, revealing the simultaneous role that moisture, heat flux, and dry air entrainment plays in PBL evolution differences over IRR and NOIRR and hence the impacts of irrigation. Moreover, this study demonstrates, compared to NOIRR, there are lowering of wind speeds over IRR. The current research also provides quantitative estimates of the impacts of IF and irrigation on L–A interactions and PBL development. In addition, while the results from this study are based on the data for 24–25 July and represents a single weather event, it has implications for local and regional climate. Such weather events, of a very similar nature, occur during different times the growing season each year, not only in Nebraska, but anywhere irrigation is applied. To further understand the link between irrigation and PBL development, it is important to have access to irrigation applications data. However, due to privacy and other concern they are not readily available. Higher-quality remotely sensed soil moisture data may assist in addressing this issue. Better quality soil moisture data would also assist in minimizing some of the biases related to estimates of fluxes and better capturing diurnal evolution of PBL processes under irrigation. In addition, future research may include PBL evolution during nonclear days and during morning and afternoon–evening transitions over irrigated land use. Subsequently, these understandings will contribute to improvements in PBL schemes. Furthermore, although the focus of this paper is not irrigation modeling, it is evident that there is room for improvement in this area of research. Irrigation applications is constrained by both socioeconomic and physical factors. Future irrigation modeling may consider both of these aspects to improve irrigation modeling which would assist in L–A interactions research in the context of irrigated land use.

Acknowledgments. The authors thank three anonymous reviewers for their valuable feedback which helped to improve this paper. This research is funded by the National Science Foundation (NSF) Grants AGS-1853390 (Rezaul Mahmood and Eric Rappin), AGS-1720477 (Udaysankar Nair), and AGS-1552487 (Roger Pielke Sr.). We would also like to acknowledge high-performance computing support from Cheyenne (doi:10.5065/D6RX99HX) provided by NCAR's Computational and Information Systems Laboratory, sponsored by the NSF. The authors thank Dallas Staley for her usual excellent editing.

REFERENCES

Adegoke, J. O., R. A. Pielke, J. Eastman, R. Mahmood, and K. G. Hubbard, 2003: Impact of irrigation of midsummer surface fluxes and temperature under dry synoptic conditions: A regional atmospheric model study of the U.S. High Plains. *Mon. Wea. Rev.*, **131**, 556–564, https://doi.org/10.1175/1520-0493(2003)131<0556:IOIOMS>2.0.CO;2.

——, R. Pielke Sr., and A. M. Carleton, 2007: Observational and modeling studies of the impacts of agriculture-related land use change on planetary boundary layer processes in the central US. *Agric. For. Meteor.*, **142**, 203–215, https://doi.org/10.1016/j.agrformet.2006.07.013.

Alter, R. E., H. C. Douglas, J. M. Winter, and E. A. Eltahir, 2018: Twentieth century regional climate change during the summer in the central United States attributed to agricultural intensification. *Geophys. Res. Lett.*, **45**, 1586–1594, https://doi.org/10.1002/2017GL075604.

Barnston, A., and P. T. Schickedanz, 1984: The effect of irrigation on warm season precipitation in the Southern Great Plains. *J. Climate Appl. Meteor.*, **23**, 865–888, https://doi.org/10.1175/1520-0450(1984)023<0865:TEOIOW>2.0.CO;2.

Benjamin, S. G., and Coauthors, 2016: A North American hourly assimilation and model forecast cycle: The Rapid Refresh. *Mon. Wea. Rev.*, **144**, 1669–1694, https://doi.org/10.1175/MWR-D-15-0242.1.

Betts, R. A., P. D. Falloon, K. K. Goldewijk, and N. Ramankutty, 2007: Biogeophysical effects of land use on climate: Model simulations of radiative forcing and large-scale temperature change. *Agric. For. Meteor.*, **142**, 216–233, https://doi.org/10.1016/j.agrformet.2006.08.021.

Brovkin, V., and Coauthors, 2013: Effect of anthropogenic land-use and land-cover changes on climate and land carbon storage in CMIP5 projections for the twenty-first century. *J. Climate*, **26**, 6859–6881, https://doi.org/10.1175/JCLI-D-12-00623.1.

Campra, P., M. Garcia, Y. Canton, and A. Palacios-Orueta, 2008: Surface temperature cooling trends and negative radiative forcing due to land use change toward greenhouse farming in southeastern Spain. *J. Geophys. Res.*, **113**, D18109, https://doi.org/10.1029/2008JD009912.

Carleton, A. M., J. Adegoke, J. Allard, D. L. Arnold, and D. J. Travis, 2001: Summer season land cover—Convective cloud associations for the midwest US "Corn Belt." *Geophys. Res. Lett.*, **28**, 1679–1682, https://doi.org/10.1029/2000GL012635.

Chen, L., and P. A. Dirmeyer, 2020: Distinct impacts of land use and land management on summer temperatures. *Front. Earth Sci.*, **8**, 245, https://doi.org/10.3389/feart.2020.00245.

Cosgrove, B. A., and Coauthors, 2003: Real-time and retrospective forcing in the North American Land Data Assimilation System (NLDAS) project. *J. Geophys. Res.*, **108**, 8842, https://doi.org/10.1029/2002JD003118.

Costa, M. H., S. N. M. Yanagi, P. J. O. P. Souza, A. Ribeiro, and E. J. P. Rocha, 2007: Climate change in Amazonia caused by soybean cropland expansion, as compared to caused by pastureland expansion. *Geophys. Res. Lett.*, **34**, L07706, https://doi.org/10.1029/2007GL029271.

DeAngelis, A., F. Dominguez, Y. Fan, A. Robock, M. D. Kustu, and D. Robinson, 2010: Evidence of enhanced precipitation due to

irrigation over the Great Plains of the United States. *J. Geophys. Res.*, **115**, D15115, https://doi.org/10.1029/2010JD013892.

Devanand, A., M. Huang, M. Ashfaq, B. Barik, and S. Ghosh, 2019: Choice of irrigation water management practice affects Indian summer monsoon rainfall and its extremes. *Geophys. Res. Lett.*, **46**, 9126–9135, https://doi.org/10.1029/2019GL083875.

Gerken, T., B. L. Ruddell, R. Yu, P. C. Stoy, and D. T. Drewry, 2019: Robust observations of land-to-atmosphere feedbacks using the information flows of FLUXNET. *Climate Atmos. Sci.*, **2**, 37, https://doi.org/10.1038/s41612-019-0094-4.

He, Y., E. Lee, and J. S. Mankin, 2020: Seasonal tropospheric cooling in Northeast China associated with cropland expansion. *Environ. Res. Lett.*, **15**, 034032, https://doi.org/10.1088/1748-9326/ab6616.

Hong, S., V. Lakshmi, E. E. Small, F. Chen, M. Tewari, and K. W. Manning, 2009: Effects of vegetation and soil moisture on the simulated land surface processes from the coupled WRF/Noah model. *J. Geophys. Res.*, **114**, D18118, https://doi.org/10.1029/2008JD011249.

Iacono, M. J., J. S. Delamere, E. J. Mlawer, M. W. Shephard, S. A. Clough, and W. D. Collins, 2008: Radiative forcing by long-lived greenhouse gases: Calculations with the AER radiative transfer models. *J. Geophys. Res.*, **113**, D13103, https://doi.org/10.1029/2008JD009944.

Johnson, B. B., C. Thompson, A. Giri, and S. Van NewKirk, 2011. Nebraska irrigation fact sheet. Dept. of Agricultural Economics, University of Nebraska–Lincoln, 6 pp.

Kennedy, A. D., X. Dong, B. Xi, S. Xie, Y. Zhang, and J. Chen, 2011: A comparison of MERRA and NARR reanalyses with the DOE ARM SGP data. *J. Climate*, **24**, 4541–4557, https://doi.org/10.1175/2011JCLI3978.1.

Kleist, D. T., D. F. Parrish, J. C. Derber, R. Treadon, W.-S. Wu, and S. Lord, 2009: Introduction of the GSI into the NCEP Global Data Assimilation System. *Wea. Forecasting*, **24**, 1691–1705, https://doi.org/10.1175/2009WAF2222201.1.

Kumar, S. V., and Coauthors, 2006: Land information system - An interoperable framework for high resolution land surface modeling. *Environ. Modell. Software*, **21**, 1402–1415, https://doi.org/10.1016/j.envsoft.2005.07.004.

Lawston, P. M., J. A. Santanello Jr., B. F. Zaitchik, and M. Rodell, 2015: Impact of irrigation methods on land surface model spinup and initialization of WRF forecasts. *J. Hydrometeor.*, **16**, 1135–1154, https://doi.org/10.1175/JHM-D-14-0203.1.

——, ——, B. Hanson, and K. Arsensault, 2020: Impacts of irrigation on summertime temperatures in the Pacific Northwest. *Earth Interact.*, **24**, 1–26, https://doi.org/10.1175/EI-D-19-0015.1.

LeMone, M. A., F. Chen, J. G. Alfieri, M. Tewari, B. Geerts, Q. Miao, R. L. Grossman, and R. L. Coulter, 2007: Influence of land cover and soil moisture on the horizontal distribution of sensible and latent heat fluxes in southeast Kansas during IHOP_2002 and CASES-97. *J. Hydrometeor.*, **8**, 68–87, https://doi.org/10.1175/JHM554.1.

Li, H., M. Wolter, X. Wang, and S. Sodoudi, 2018: Impact of land cover data on the Simulation of urban heat island for Berlin using WRF coupled with bulk approach of Noah-LSM. *Theor. Appl. Climatol.*, **134**, 67–81, https://doi.org/10.1007/s00704-017-2253-z.

Loveland, T. R., and R. Mahmood, 2014: A design for a sustained assessment of climate forcing and feedbacks related to land use and land cover change. *Bull. Amer. Meteor. Soc.*, **95**, 1563–1572, https://doi.org/10.1175/BAMS-D-12-00208.1.

Mahmood, R., and K. G. Hubbard, 2002: Anthropogenic land-use change in the North American tall grass-short grass transition and modification of near-surface hydrologic cycle. *Climate Res.*, **21**, 83–90, https://doi.org/10.3354/cr021083.

——, ——, and C. Carlson, 2004: Modification of growing season surface temperature records in the northern Great Plains due to land use transformation: Verification of modeling results and implication for global climate change. *Int. J. Climatol.*, **24**, 311–327, https://doi.org/10.1002/joc.992.

——, R. A. Pielke, and K. G. Hubbard, 2006: Land use/land cover change and its impacts on climate. *Global Planet. Change*, **54**, vii, https://doi.org/10.1016/j.gloplacha.2006.05.004.

——, K. G. Hubbard, R. Leeper, and S. A. Foster, 2008: Increase in near surface atmospheric moisture content due to land use changes: Evidence from the observed dew point temperature data. *Mon. Wea. Rev.*, **136**, 1554–1561, https://doi.org/10.1175/2007MWR2040.1.

——, and Coauthors, 2010: Impacts of land use land cover change on climate and future research priorities. *Bull. Amer. Meteor. Soc.*, **91**, 37–46, https://doi.org/10.1175/2009BAMS2769.1.

——, and Coauthors, 2014: Land cover changes and their biogeophysical effects on climate. *Int. J. Climatol.*, **34**, 929–953, https://doi.org/10.1002/joc.3736.

——, and Coauthors, 2020: The total solar eclipse of 2017: Meteorological observations from a statewide mesonet and atmospheric profiling systems. *Bull. Amer. Meteor. Soc.*, **101**, E720–E737, https://doi.org/10.1175/BAMS-D-19-0051.1.

Meehl, G. A., R. Moss, K. E. Taylor, V. Eyring, R. J. Stouffer, S. Bony, and B. Stevens, 2014: Climate model intercomparison: Preparing for the next phase. *Eos, Trans. Amer. Geophys. Union*, **95**, 77–78, https://doi.org/10.1002/2014EO090001.

Melillo, J. M., T. Richmond, and G. W. Yohe, 2014: *Climate Change Impacts in the United States: The Third National Climate Assessment.* U.S. Global Change Research Program, 841 pp.

Mesinger, F., and Coauthors, 2006: North American Regional Reanalysis. *Bull. Amer. Meteor. Soc.*, **87**, 343–360, https://doi.org/10.1175/BAMS-87-3-343.

Nair, U. S., and Coauthors, 2019: Influence of land cover and soil moisture based brown ocean effect on an extreme rainfall event from a Louisiana Gulf Coast tropical system. *Sci. Rep.*, **9**, 17136, https://doi.org/10.1038/s41598-019-53031-6.

Nakanishi, M., and H. Niino, 2006: An improved Mellor–Yamada level 3 model: Its numerical stability and application to a regional prediction of advecting fog. *Bound.-Layer Meteor.*, **119**, 397–407, https://doi.org/10.1007/s10546-005-9030-8.

——, and ——, 2009: Development of an improved turbulence closure model for the atmospheric boundary layer. *J. Meteor. Soc. Japan*, **87**, 895–912, https://doi.org/10.2151/jmsj.87.895.

National Agricultural Statistics Service, 2017: NASS - Quick Stats. USDA National Agricultural Statistics Service, accessed 28 May 2022, https://data.nal.usda.gov/dataset/nass-quick-stats.

Nikiel, C. A., and E. A. Eltahir, 2019: Summer climate change in the Midwest and Great Plains due to agricultural development during the twentieth century. *J. Climate*, **32**, 5583–5599, https://doi.org/10.1175/JCLI-D-19-0096.1.

O'Neill, P. E., S. Chan, E. G. Njoku, T. Jackson, R. Bindlish, and J. Chaubell, 2020: SMAP Enhanced L3 Radiometer Global Daily 9 km EASE-Grid Soil Moisture, Version 4. NASA National Snow and Ice Data Center Distributed Active Archive Center, accessed 30 May 2020, https://doi.org/10.5067/NJ34TQ2LFE90.

Ozdogan, M., and G. Gutman, 2008: A new methodology to map irrigated areas using multi-temporal MODIS and ancillary data: An application example in the continental US. *Remote*

Sens. Environ., **112**, 3520–3537, https://doi.org/10.1016/j.rse.2008.04.010.

Peters-Lidard, C. D., and Coauthors, 2007: High-performance Earth system modeling with NASA/GSFC's Land Information System. *Innov. Syst. Softw. Eng.*, **3**, 157–165, https://doi.org/10.1007/s11334-007-0028-x.

Pielke, R. A., Sr., J. Adegoke, A. Beltrán-Przekurat, C. A. Hiemstra, J. Lin, U. S. Nair, D. Niyogi, and T. E. Nobis, 2007: An overview of regional land-use and land-cover impacts on rainfall. *Tellus*, **59B**, 587–601, https://doi.org/10.1111/j.1600-0889.2007.00251.x.

——, and Coauthors, 2011: Land use/land cover changes and climate: Modeling analysis and observational evidence. *Wiley Interdisc. Rev.: Climate Change*, **2**, 828–850, https://doi.org/10.1002/wcc.144.

——, R. Mahmood, and C. McAlpine, 2016: Land's complex role in climate change. *Phys. Today*, **69**, 40–46, https://doi.org/10.1063/PT.3.3364.

Pitman, A. J., and Coauthors, 2009: Uncertainties in climate responses to past land cover change: First results from the LUCID intercomparison study. *Geophys. Res. Lett.*, **36**, L14814, https://doi.org/10.1029/2009GL039076.

Puma, M. J., and B. I. Cook, 2010: Effects of irrigation on global climate during the 20th century. *J. Geophys. Res.*, **115**, D16120, https://doi.org/10.1029/2010JD014122.

Qian, Y., M. Huang, B. Yang, and L. K. Berg, 2013: A modeling study of irrigation effects on surface fluxes and land–air–cloud interactions in the Southern Great Plains. *J. Hydrometeor.*, **14**, 700–721, https://doi.org/10.1175/JHM-D-12-0134.1.

——, and Coauthors, 2020: Neglecting irrigation contributes to the simulated summertime warm-and-dry bias in the central United States. *npj Climate Atmos. Sci.*, **3**, 31, https://doi.org/10.1038/s41612-020-00135-w.

Rabin, R. M., S. Stadler, P. J. Wetzel, D. J. Stensrud, and M. Gregory, 1990: Observed effects of landscape variability on convective clouds. *Bull. Amer. Meteor. Soc.*, **71**, 272–280, https://doi.org/10.1175/1520-0477(1990)071<0272:OEOLVO>2.0.CO;2.

Rappin, E., and Coauthors, 2021: The Great Plains Irrigation Experiment (GRAINEX). *Bull. Amer. Meteor. Soc.*, **102**, E1756–E1785, https://doi.org/10.1175/BAMS-D-20-0041.1.

Rodgers, W., R. Mahmood, R. Leeper, and J. Yan, 2018: Land cover change, surface mining, and their impacts on a heavy rain event in the Appalachia. *Ann. Amer. Assoc. Geogr.*, **108**, 1187–1209, https://doi.org/10.1080/24694452.2018.1460249.

Salmon, J. M., M. A. Friedl, S. Frolking, D. Wisser, and E. M. Douglas, 2015: Global rain-fed, irrigated, and paddy croplands: A new high resolution map derived from remote sensing, crop inventories and climate data. *Int. J. Appl. Earth Obs. Geoinf.*, **38**, 321–334, https://doi.org/10.1016/j.jag.2015.01.014.

Santanello, J. A., Jr., C. D. Peters-Lidard, S. V. Kumar, C. Alonge, and W.-K. Tao, 2009: A modeling and observational framework for diagnosing local land–atmosphere coupling on diurnal time scales. *J. Hydrometeor.*, **10**, 577–599, https://doi.org/10.1175/2009JHM1066.1.

——, ——, and ——, 2011: Diagnosing the sensitivity of local land–atmosphere coupling via the soil moisture–boundary layer interaction. *J. Hydrometeor.*, **12**, 766–786, https://doi.org/10.1175/JHM-D-10-05014.1.

Segal, M., J. R. Garratt, R. A. Pielke, W. E. Schreiber, A. Rodi, G. Kallos, and J. Weaver, 1989: The impact of crop areas in northeast Colorado on midsummer mesoscale thermal circulations. *Mon. Wea. Rev.*, **117**, 809–825, https://doi.org/10.1175/1520-0493(1989)117<0809:TIOCAI>2.0.CO;2.

Sen Roy, S., R. Mahmood, A. I. Quintanar, and A. Gonzalez, 2011: Impacts of irrigation on dry Season precipitation in India. *Theor. Appl. Climatol.*, **104**, 193–207, https://doi.org/10.1007/s00704-010-0338-z.

Skamarock, W. C., and Coauthors, 2019: A description of the Advanced Research WRF Model version 4. NCAR Tech. Note NCAR/TN-556+STR, 145 pp., https://doi.org/10.5065/1dfh-6p97.

Szilagyi, J., and T. E. Franz, 2020: Anthropogenic hydrometeorological changes at a regional scale: Observed irrigation–precipitation feedback (1979–2015) in Nebraska, USA. *Sustain. Water Resour. Manag.*, **6**, 1, https://doi.org/10.1007/s40899-020-00368-w.

Tewari, M., and Coauthors, 2004: Implementation and verification of the unified NOAH land surface model in the WRF model. *20th Conf. on Weather Analysis and forecasting/16th Conf. on Numerical Weather Prediction*, Seattle, WA, Amer. Meteor. Soc., 14.2a, https://ams.confex.com/ams/84Annual/techprogram/paper_69061.htm.

Thiery, W., and Coauthors, 2020: Warming of hot extremes alleviated by expanding irrigation. *Nat. Comm.*, **11**, 290, https://doi.org/10.1038/s41467-019-14075-4.

Thompson, G., P. R. Field, R. M. Rasmussen, and W. D. Hall, 2008: Explicit forecasts of winter precipitation using an improved bulk microphysics scheme. Part II: Implementation of a new snow parameterization. *Mon. Wea. Rev.*, **136**, 5095–5115, https://doi.org/10.1175/2008MWR2387.1.

Valmassoi, A., J. Dudhia, S. Di Sabatino, and F. Pilla, 2020: Regional climate impacts of irrigation in northern Italy using a high resolution model. *Atmosphere*, **11**, 72, https://doi.org/10.3390/atmos11010072.

Van Heerwaarden, C. C., J. Vilà-Guerau de Arellano, A. F. Moene, and A. A. Holtslag, 2009: Interactions between dry-air entrainment, surface evaporation and convective boundary-layer development. *Quart. J. Roy. Meteor. Soc.*, **135**, 1277–1291, https://doi.org/10.1002/qj.431.

Van Weverberg, K., and Coauthors, 2018: CAUSES: Attribution of surface radiation biases in NWP and climate models near the U.S. Southern Great Plains. *J. Geophys. Res. Atmos.*, **123**, 3612–3644, https://doi.org/10.1002/2017JD027188.

Wei, J., P. A. Dirmeyer, D. Wisser, M. C. Bosilovich, and D. M. Mocko, 2013: Where does the irrigation water go? An estimate of the contribution of irrigation to precipitation using MERRA. *J. Hydrometeor.*, **14**, 275–289, https://doi.org/10.1175/JHM-D-12-079.1.

Whitaker, J. S., T. M. Hamill, X. Wei, Y. Song, and Z. Toth, 2008: Ensemble data assimilation with the NCEP Global Forecast System. *Mon. Wea. Rev.*, **136**, 463–482, https://doi.org/10.1175/2007MWR2018.1.

Winchester, J., R. Mahmood, W. Rodgers, F. Hossain, E. Rappin, J. Durkee, and T. Chronis, 2017: A model-based assessment of potential impacts of man-made reservoirs on precipitation. *Earth Interact.*, **21**, https://doi.org/10.1175/EI-D-16-0016.1.

Wu, W.-S., R. J. Purser, and D. F. Parrish, 2002: Three-dimensional variational analysis with spatially inhomogeneous covariances. *Mon. Wea. Rev.*, **130**, 2905–2916, https://doi.org/10.1175/1520-0493(2002)130<2905:TDVAWS>2.0.CO;2.

Wyngaard, J. C., 2004: Toward numerical modeling in the "terra incognita." *J. Atmos. Sci.*, **61**, 1816–1826, https://doi.org/10.1175/1520-0469(2004)061<1816:TNMITT>2.0.CO;2.

Xu, X., Y. Jiang, M. Liu, Q. Huang, and G. Huang, 2019: Modeling and assessing agro-hydrological processes and irrigation water

saving in the middle Heihe River basin. *Agric. Water Manage.*, **211**, 152–164, https://doi.org/10.1016/j.agwat.2018.09.033.

Yang, Z., F. Dominguez, X. Zeng, H. Hu, H. Gupta, and B. Yang, 2017: Impact of irrigation over the California Central Valley on regional climate. *J. Hydrometeor.*, **18**, 1341–1357, https://doi.org/10.1175/JHM-D-16-0158.1.

——, and Coauthors, 2019: Irrigation impact on water and energy cycle during dry years over the United States using convection-permitting WRF and a dynamical recycling model. *J. Geophys. Res. Atmos.*, **124**, 11 220–11 241, https://doi.org/10.1029/2019JD030524.

Zeng, J., K.-S. Chen, H. Bi, and Q. Chen, 2016: A preliminary evaluation of the SMAP radiometer soil moisture product over United States and Europe using ground-based measurements. *IEEE Trans. Geosci. Remote Sens.*, **54**, 4929–4940, https://doi.org/10.1109/TGRS.2016.2553085.

Zhang, C., S. Xie, S. A. Klein, H.-Y. Ma, S. Tang, K. Van Weverberg, C. J. Morcrette, and J. Petch, 2018: CAUSES: Diagnosis of the summertime warm bias in CMIP5 climate models at the ARM Southern Great Plains site. *J. Geophys. Res. Atmos.*, **123**, 2968–2992, https://doi.org/10.1002/2017JD027200.